Ferroelectricity of stress-free and strained pure SrTiO_3 revealed by ab initio calculations with hybrid and density functionals

Watanabe, Yukio
Department of Physics, Kyushu University

出版情報：Physical Review B. 99, pp.064107-1-064107-14, 2019-02-19. American Physical Society
バージョン：

Ferroelectricity of stress-free and strained pure $SrTiO_3$ revealed by *ab initio* calculations with hybrid and density functionals

Yukio Watanabe
Department of Physics, Kyushu University, Fukuoka 819-0395, Japan

(Received 29 August 2018; revised manuscript received 13 December 2018; published 19 February 2019)

The properties of stress-free and biaxially strained stoichiometric $SrTiO_3$ in the absence and presence of antiferrodistortive (AFD) distortion were calculated *ab initio*. To obtain reliable results, multiple exchange correlation (XC) functionals, including the Heyd-Scuseria-Ernzerhof (HSE) hybrid functional, were used. HSE was the primary XC functional, while another functional provided a good lower bound of ferroelectricity (FE). The reliability of the calculations was further reinforced by the calculations of the strain and AFD dependence. In contrast with previous works, we show that the ferroelectric phase (C_{4v}^1, C_{4v}^{10}) is more stable in the absence of quantum and thermal fluctuations than the paraelectric phase (O_h^1, D_{4h}^{18}), even for the stress-free case, and clarify the properties of these FE phases. The energy gain of stress-free FE, in comparison with the thermal and quantum fluctuation energy, indicates that a paraelectric phase emerges at room temperature by thermal fluctuations, but is near 0 K marginally close to the FE phase, which aligns with the experimental incipient FE. This implies that the paraelectricity of stress-free $SrTiO_3$ in experiments contains incoherent atomic-scale FE regions. These results are consistent with the FE microregions (FMR), signatures of polar disorders, and the emergence of FE in $SrTiO_3$ due to impurities and defects. The value of spontaneous polarization P_S could reach $10\,\mu C/cm^2$ in the absence of fluctuations, even for the stress-free case. In view of the earlier theory of the carrier layer at polar discontinuities, the present results may explain the conduction at the interfaces of the $LaAlO_3/SrTiO_3$. In addition, an "enhancement of FE due to symmetry constriction" is proposed as an additional mechanism to the strain-enhanced FE in the epitaxial effect. For large compressive strain, e.g., 2%, the Perdew-Burke-Ernzerhof density functional for solids (PBEsol) yielded properties with $P_S > 20\,\mu C/cm^2$, agreeing with HSE, and therefore is usable as a practical substitute of HSE for $SrTiO_3$.

DOI: 10.1103/PhysRevB.99.064107

I. INTRODUCTION

An incipient ferroelectric $SrTiO_3$ exhibits quantum paraelectricity as a ground-state property due to quantum mechanical fluctuations [1,2] and has intriguing properties, including a gigantic relative permittivity surpassing 10^5 [3], as well as high photolysis [4], catalysis, and electrocatalysis performance [5]. $SrTiO_3$ becomes ferroelectric (FE) by very small perturbations, which are manifested in the form of exotic domain walls [6], two-dimensional conduction at the insulator interface [7–14], and ferrolike properties at room temperature (RT) at surfaces and in nanodots [15,16]. Here, polar discontinuity is considered important for these conductions [7–14], providing a universal mechanism at the ferroelectric/insulator interface and the charged domain boundaries as in earlier predictions [17,18].

Stress-free $SrTiO_3$ is cubic at RT with its unit cell consisting of five atoms and O_h^1 symmetry (Table I). Stress-free $SrTiO_3$ undergoes an antiferrodistortive (AFD) structural phase transition below ∼105–110 K by the R_{25} (Γ_{25}) phonon freezing [19–27]. The unit cell is tetragonal with D_{4h}^{18} symmetry consisting of 20 atoms. In the experiments of the D_{4h}^{18} paraelectric (PE), ferroelectricity (FE) emerges by a small stress [28–30], a tiny amount of impurity [3,31], or an electric field [32,33]. In addition, a nanoscopic inhomogeneity called a FE microregion (FMR) is attributed to unintended impurities [34–38], where we can regard FMR as the polar nanoregion (PNR) found in relaxors.

The stresses from the interface, defects, and impurities are considered essential for the aforementioned properties. Therefore, we study the ground state in the presence and absence of stress. For this, the properties in the absence of thermal and quantum mechanical fluctuations are essential and have been studied using various approaches including *ab initio* calculations [39–45].

The *ab initio* calculations of stress effects on $SrTiO_3$ using theoretical unit cells have shown that the stress-free RT phase is PE and a large strain of $>\sim 0.007$ induces FE [39–41]. In contrast, Sai and Vanderbilt [42] and LaSota *et al.* [43] predicted the soft-mode instability from a PE to a FE phase using experimental stress-free unit-cell parameters. These studies used the local density functional approximation (LDA) as the exchange-correlation (XC) energy part of the *ab initio* calculation. In addition, studies using recent XC functionals [44,45] suggested the existence of a soft-mode phonon instability to a FE phase.

Because the ground state of stress-free stoichiometric $SrTiO_3$ by *ab initio* calculations remains unresolved, the strain effect on FE is also unresolved. In addition, the properties of the stress-free and strained FE phase such as the spontaneous polarization P_S and free energy remain unclarified by *ab initio* calculations. *The present paper aims to resolve these issues and clarify the properties of the stress-free and strained FE phase with* $P_S//c$ *axis* (C_{4v}^1,C_{4v}^{10}) *in the absence of thermal and quantum mechanical fluctuations.*

Here, the examinations of the previous calculations [39–43,45–49] show the acute importance of the lattice constants for FE of $SrTiO_3$. The experiments also show that a 0.1% difference of the ratio of the c-axis and a-axis lattice constant (c/a) is significant for FE in $SrTiO_3$ [28,29]. However, we cannot use experimental lattice constants for the calculations of the properties of a stress-free FE phase because they are experimentally unknown.

Therefore, we have to theoretically obtain very accurate lattice constants. However, an agreement within 0.1% of the *ab initio* calculated lattice constants with the experimental ones is rarely achieved. To overcome this, we note the critical dependence of the lattice parameters on the XC functionals [45–49].

To attain accuracy, we used a fourfold approach: (1) The XC functional that yielded the best agreement of theoretical lattice parameters of $SrTiO_3$ with experimental ones was used. (2) A good lower bound of FE of $SrTiO_3$ was estimated by use of the second-best XC functional. (3) The consistency of the calculations of strained $SrTiO_3$ with the experiments [28–30,50] was examined. (4) The AFD angle (φ) dependence of FE was calculated.

The examined functionals in the present paper include the Perdew-Burke-Ernzerhof functional for solids (PBEsol) [51] that is currently a standard XC functional and the Heyd-Scuseria-Ernzerhof functional (HSE) [52] that is a hybrid XC functional and is considered to estimate accurate internal forces [45,49]. Here, the basic and clear examination of the accuracy is the comparison of the theoretical and experimental lattice parameters: In Sec. III, the difference between the $SrTiO_3$ lattice constants given by experiments and those calculated with PBEsol and HSE was smaller than the experimental variations [23–25].

The examinations of lattice constants in Sec. III and Appendix A suggest the strategy for high accuracy and reliability: PBEsol was the best estimate for the O_h^1 phase or a good *lower bound of FE*, while it was a *lower bound of FE* for the D_{4h}^{18} phase. HSE was the best estimate for the O_h^1 phase or a good *upper bound of FE*, while it was the best estimate for the D_{4h}^{18} phase. These views were also supported by the comparison with the strain experiments [28,29] in Secs. IV and V and the φ dependence in Appendix A. Therefore, the calculations are reliable when both PBEsol and HSE results are mutually consistent.

These examinations have resolved the aforementioned controversy over stress-free $SrTiO_3$, showing definitely that the FE phases have lower free energy than the standard PE phases and, therefore, can exist in the absence of fluctuations. That is, the free energy of the C_{4v}^1 FE phase is lower than that of the O_h^1 PE phase, and the free energy of the C_{4v}^{10} FE phase is lower than that of the D_{4h}^{18} PE phase (Table I). Because the difference between the PE and the FE phases is much smaller than the energy scale of the 300 K thermal and quantum fluctuations [1,2], the present results are consistent with the PE phases observed in experiments. That is, the experimentally observed PE state can be considered an assembly of atomic-scale FE domains or different phases under the assumption that the effect of quantum fluctuation is the destruction or randomization of long-range orders.

TABLE I. Symmetry of the RT and the 105 K phases. The experimentally observed stress-free RT phase is cubic (O_h^1) and all other phases are tetragonal. D_{4h}^1 appears by biaxial strain. No FE phase with $P_S \perp c$ is examined in the present study.

	Paraelectric	Ferroelectric $P_S//c$
RT phase	O_h^1 ($Pm3m$) [D_{4h}^1($P4/mmm$)]	C_{4v}^1 ($P4mm$)
105 K phase	D_{4h}^{18} ($I4/mcm$)	C_{4v}^{10} ($I4cm$)

In addition, the strain effects were shown to surpass the thermal and quantum fluctuations, which explains the experiments of strain effects in single crystals [28–30] and thin films [50]. This suggests the contribution of FE to the various properties of $SrTiO_3$/insulator interfaces [7,8,10–12] and interprets the polar catastrophe [14] as polar discontinuities, as predicted and demonstrated previously [17,18].

In the following, we collectively call the O_h^1, D_{4h}^1, and C_{4v}^1 phases the *RT phase* and call the D_{4h}^{18} and C_{4v}^{10} phases the *105 K phase* (Table I). This naming is also applied to FE and PE phases; for example, the RT and 105 K FE phases stand for the C_{4v}^1 and C_{4v}^{10} phase FE, respectively. The free energy and lattice constants of the 105 K phase will be reported mostly for a "pseudocubic unit cell" that consists of five atoms [Fig. 1(b)]. Only uniform perturbative displacements of ions for $P_S//c$ were studied. All the *ab initio* calculations below were the standard ones that neglected thermal and quantum fluctuations, even if not explicitly specified.

This paper is organized as follows: Sec. II describes the technical details of our calculations and definitions of pseudocubic cell, symmetry, strain u, and crystal axes. Section III examines XC functionals. Sections IV and V examine the RT and 105 K phases, respectively. Section VI examines the FE shown in Secs. IV and V, in view of reliability of the calculations, the effects of quantum and thermal fluctuations, and the P_S-assisted impurity conductance of the $LaAlO_3/SrTiO_3$ [13,14]. Section VII summarizes the results. Appendix A reports the φ dependence of the 105 K phases for the examination of the FE in stress-free $SrTiO_3$. Appendix B reports the XC-functional dependence of FE distortions and electronic charge distributions. Appendix C reports strain- and symmetry-constriction-induced P_S at $LaAlO_3/SrTiO_3$ as a support of the present results.

II. TECHNICAL DETAILS AND DEFINITION OF CRYSTAL AXES

The $[100]_{RT}$ and $[010]_{RT}$ axes represent the a axes a_{RT} of the RT phases, where the suffix "RT" stands for the RT phases (O_h^1, D_{4h}^1, C_{4v}^1) and the direction of each axis of these phases is mutually parallel. The c axis of the tetragonal 20-atom unit cell of the 105 K phases c_t is approximately equal to $2c_{RT}$ (c_{RT}: c axis of the RT phases) and $[001]_t//[001]_{RT}$, where the suffix "t" stands for the tetragonal unit cell of the 105 K phases (D_{4h}^{18}, C_{4v}^{10}). The a axes of the tetragonal unit cell of the 105 K phases a_t is nearly equal to $\sqrt{2}a_{RT}$ with $[100]_t//[\bar{1}10]_{RT}$ and $[010]_t//[110]_c$ [Fig. 1(b)]. Denoting the pseudocubic cell by the suffix "pc," $a_{pc} \approx a_{RT}$, $c_{pc} \approx c_{RT}$, $[100]_{pc}//[100]_{RT}$,

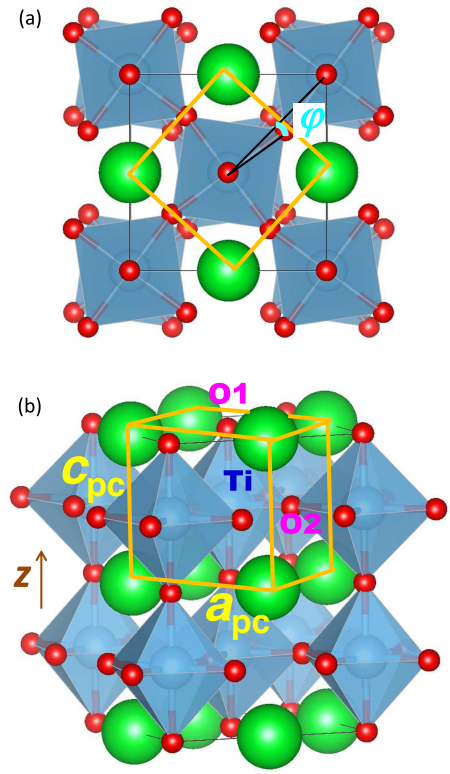

FIG. 1. (a) Top and (b) side schematic view of 105 K PE phase $SrTiO_3$ D_{4h}^{18} ($I4/mcm$) unit cell, showing the AFD distortion of octahedral oxygens around the c axis with rotation angle φ. Orange square frames show a "pseudocubic unit cell," and the letters a_{pc} and c_{pc} indicates the a and c axis of the pseudocubic unit cell, respectively. The z axis is parallel to the c axes. Large and small spheres and diamonds represent Sr, O, and Ti atoms, respectively, where Ti atoms are indicated with "Ti." Two inequivalent positions of O atoms are indicated by "O1" and "O2."

$[010]_{pc}//[010]_{RT}$, and $[001]_{pc}//[001]_{RT}$. Therefore, we use $[100]_{pc}$ and $[010]_{pc}$ also for $[100]_{RT}$ and $[010]_{RT}$, respectively. Because $[001]_t//[001]_{RT}$ and $[001]_{pc}//[001]_{RT}$, we always use [001] or c for these directions.

AFD is represented by the rotation of oxygens (O2) by an angle φ in Fig. 1(a). In epitaxial $SrTiO_3$ film experiments, $P_S//[001]$ appears by *biaxial in-plane* stress [50]. We assume that the in-plane biaxial stress is in the plane formed by the $[100]_{pc}$ and $[010]_{pc}$ axes, where the stresses along the two axes are the same.

We used LDA, HSE (HSE06) [52,53], and HSE for solid (HSEsol) [54] as hybrid functionals, the Tao-Perdew-Staroverov-Scuseria functional (TPSS) [55] as meta-GGA, and TPSS with Hubbard-like local potential [56] (TPSS+U). As the generalized gradient approximations (GGA), PBEsol [51] and PBE [57] were employed. The parameter μ for a screening length in HSE06 and HSEsol is the default value ($0.2\,\text{Å}^{-1}$). In TPSS+U, $U = 8$ eV and an exchange term $J = 0$ on oxygen atoms [49]. All calculations were performed using the projector augmented wave (PAW) method [58] as implemented in the Vienna *ab initio* simulation package VASP [59] with a plane-wave energy cutoff of 650 eV. Different GGA and LDA PAW potentials were tested, and the difference between the results by these potentials was negligible in comparison with those between different XC functionals. Therefore, the results below use one set of PAW potential.

For the RT phases, a Monkhorst-Pack [60] mesh of $6 \times 6 \times 6$ for the Brillouin-zone integration was used in geometry relaxation and Berry phase calculation of P_S. After the relaxation of the RT phases, the calculated forces were always less than 0.5 meV/Å. These results by LDA and PBEsol were the same as those calculated with the Monkhorst-Pack mesh of $11 \times 11 \times 11$ and the calculated forces <0.01 meV/Å.

For the 105 K phases, except for HSE, a Monkhorst-Pack [60] mesh of $8 \times 8 \times 6$ for the Brillouin-zone integration was used in geometry relaxation and Berry phase calculation of P_S. After the relaxation, the calculated forces were always <0.01 meV/Å and, near the minimum free energy, <0.001 meV/Å. In the case of HSE, a Monkhorst-Pack [60] mesh of $6 \times 6 \times 4$ for the Brillouin-zone integration was used in geometry relaxation and Berry phase calculation of P_S, with the calculated force <0.5 meV/Å. This criterion was sufficient because the energy differences among different phases estimated by HSE were of a few orders of magnitude larger than those estimated by PBEsol.

As for FE distortions, small uniform displacements of ions $//c$, i.e., Slater-mode-like displacements $//c$, are applied as an initial perturbation for $P_S//c$. Consequently, the RT and 105 K phases were calculated under the symmetry constraint of C_{4v}^1 ($\supset D_{4h}^1 \supset O_h^1$) and C_{4v}^{10} ($\supset D_{4h}^{18}$), respectively.

As for *stress-free* RT and 105 K PE, *ab initio* calculations with multiple XC functionals are reported by Wahl *et al.* [45], which are favorably compared with the present calculations: The present PBEsol calculations for stress-free PE phase $SrTiO_3$ agree completely with Wahl *et al.* [45], including zone-center phonon frequencies. The present results for stress-free PE phases by LDA and HSE06 agreed well with Wahl *et al.* [45], including the zone-center phonon frequencies, although the parameters and the PAW potentials are different from Wahl *et al.* [45]. As another consistency check, we calculated the properties of the 105 K phases using LDA with experimental lattice constants [23], which were consistent with Sai and Vanderbilt [42] and LaSota *et al.* [43].

For RT phases, the strain u is defined by $u \equiv (a - a_{RT0})/a_{RT0}$, where the theoretical a-axis lattice constant a_{RT0} of the stress-free O_h^1 PE phase is calculated with *each* XC functional. For 105 K phases, the strain u is defined by $u \equiv (a - a_{t0})/a_{t0}$, where the theoretical a-axis lattice constant a_{t0} of the stress-free D_{4h}^{18} PE phase is calculated with *each* XC functional. Similarly, φ_0 is the AFD angle φ [Fig. 1(b)] under the stress-free condition calculated with each XC functional.

In the calculations of strain dependence, all the lattice parameters were fully optimized except for a given a-lattice constant. In the calculations of the AFD angle (φ) dependence, all the lattice parameters were fully optimized except for the in-plane coordinates of the oxygen atoms (O2) in the TiO_2 plane; all the $|\varphi|$ in Fig. 1(b) were fixed and the same for the Ti-O2 bonds. Otherwise, all ion positions were theoretically fully optimized for a given symmetry. Unless otherwise stated, the properties given by these calculations were of the lattice optimized fully with *each* XC functional. No isotope effect was included.

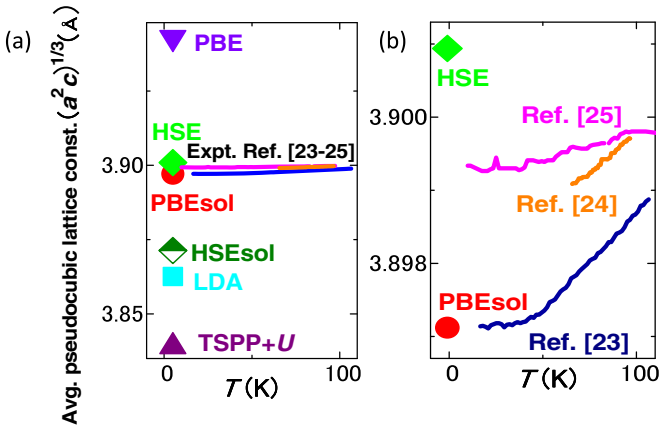

FIG. 2. (a) Comparison of theoretical lattice constant of RT PE phase $SrTiO_3$ (cubic: O_h^1) with experimental average lattice constant of pseudocubic unit cell $a^{2/3}c^{1/3}$. Filled red circles, filled green diamonds, dark half-filled green diamonds, light blue squares, purple triangles, and inverted violet triangles represent the results of PBEsol, HSE, LDA, TPSS+U, and PBE, respectively. This convention for symbols is used throughout. The lines represent experimental values [23–25]. (b) Enlarged plot. In (a) and (b), the experimental average lattice constants of the 105 K PE phase (D_{4h}^{18}) are compared with the theoretical ones of the O_h^1 PE phase. This is because the D_{4h}^{18} PE phase is very close to the O_h^1 PE phase having the ratio of the experimental c- and a-lattice constant <1.0016 [23,25], and the effect of the unit-cell volume is known to dominate in the results of *ab initio* calculations. In Appendix A, the experimental lattice constants of the D_{4h}^{18} PE phase are compared with those theoretical ones.

III. SELECTION OF XC FUNCTIONAL

The importance of the accurate estimations of the lattice constants for P_S or FE is established [42,43,45–49]. Here, FE can be represented by P_S because the free-energy gain of the FE phase is a single-valued function of $|P_S|$ (Ref. [49] and Sec. VI). In the case of $BaTiO_3$, the theoretical P_S increased with the theoretical c-lattice constant, and all P_S's calculated with four different XC functions using the experimental lattice constants agreed with the experimental P_S within 8% [49]. In addition, all the P_S's calculated with six different XC functions using the lattice constants of $BaTiO_3$ given by PBEsol agreed mutually within ±2% [49]. Therefore, we use lattice constants for the estimation of the accuracy for FE.

In Fig. 2(a), the lattice constants of the stress-free cubic phase (O_h^1) calculated with different XC functionals are compared with experiments [23–25]. The lattice constants calculated with PBEsol and HSE agree well with the experimental average lattice constant of pseudocubic cell $(a^2c)^{1/3}$ [23–25], far better than LDA, HSEsol, TPSS+U, and PBE. TPSS (not shown in Fig. 2) deviated more from experiments than TPSS+U.

An enlarged view in Fig. 2(b) shows that the lattice constant calculated with PBEsol is 0.0005% and 0.055% lower than experimental $(a^2c)^{1/3}$ by Okazaki and Kawaminami [23] and Loetzsch *et al.* [25], respectively. The lattice constant calculated with HSE is 0.098% and 0.043% higher than the experimental $(a^2c)^{1/3}$ by Okazaki and Kawaminami [23] and Loetzsch *et al.* [25], respectively. This suggests that PBEsol is expected to be accurate or underestimate FE of the RT phases slightly and HSE is expected to be accurate or slightly overestimate the FE of the RT phases (Table I).

Because the lattice constants of the D_{4h}^{18} PE phase by HSE agreed well with experimental ones in Sec. V and Appendix A, HSE is considered accurate also for the 105 K phases.

IV. RT PHASES

The LDA calculations that use theoretical lattice constants have shown that the stress-free RT phase is PE and that FE emerges for $u < -0.007$ [39–41], which is confirmed by the present LDA and HSEsol calculations in Fig. 3(a).

In the experiments of Fujii *et al.* [29], the 105 K PE phase (D_{4h}^{18}) changed to FE with $P_S \perp [001]$ at 2 K by a uniaxial stress of $1.2 \times 10^8\,\mathrm{Nm}^{-2}$ along $[010]_{pc}$. The corresponding strain ε_{xx} is estimated to be -0.0004 using the experimental and *ab initio* elastic compliances $C_{11} = 31.7 \times 10^{10}\,\mathrm{Nm}^{-2}$ and $C_{12} = 7.1 \times 10^{10}\,\mathrm{Nm}^{-2}$ [20,61–63]. In the experiments of Uwe and Sakudo [28], the 105 K PE phase (D_{4h}^{18}) changed to FE with $P_S // [001]$ at 2 K by a uniaxial stress of $5.4 \times 10^8\,\mathrm{Nm}^{-2}$ along $[110]_{pc}$. The corresponding strains ε_{xx} and ε_{yy} are estimated to be approximately > -0.0011 $(-0.0011/2)$ [Fig. 3(a)] [20,61–63].

This estimation is deduced as follows: The dielectric measurements (Fig. 2 of Ref. [28]) indicated that the uniaxial stress along $[110]_{pc}$ elongated the c-lattice constant and slightly elongated the lattice constant along $[1\bar{1}0]_{pc}$. Denoting the contraction of the $[110]_{pc}$ lattice constant and the elongation of the $[1\bar{1}0]_{pc}$ lattice constant by $-\beta < 0$ and $\delta > 0$, respectively, we assume $\beta > \delta$. The contraction of two a-lattice constants is approximately $\{[a(1-\beta)/\sqrt{2}]^2+[a(1+\delta)/\sqrt{2}]^2\}^{1/2}/a - 1 \approx -(\beta-\delta)/2$, which means $|u| = |\varepsilon_{xx}| = |\varepsilon_{yy}| < b/2 = 0.0011/2 < \beta/2 = 0.0011/2$. Therefore, 0.0011 (or 0.0011/2) is considered as an upper bound of the critical *biaxial* in-plane strain $|u_c|$ for the emergence of P_S in the *presence* of the AFD distortion and thermal/quantum fluctuations. In the *absence* of these fluctuations, the critical biaxial in-plane strain should be smaller than this estimate.

These experimental critical ε_{xx} and ε_{yy} for $P_S // [001]$ are ~5–10 times smaller than the critical ε_{xx} and ε_{yy} given by the present and previous LDA [39–41] and the present HSEsol calculations [Fig. 3(a)]. Figure 3(a) also shows that LDA and HSEsol predicted that the stress-free RT phase was a PE phase in the absence of thermal and quantum fluctuations. On the contrary, PBEsol and HSE predicted that it was a FE phase in the absence of these fluctuations, having substantial $P_S = 7.3$ and $16.5\,\mu\mathrm{C/cm}^2$, respectively. In addition, the FE phase instability of the Slater modes of the O_h^1 phase [imaginary frequency $= 3.39\,\mathrm{meV}$ $(27.3\,\mathrm{cm}^{-1})$] was shown by PBEsol that gives a lower bound of FE.

Thus, the mutually opposing theoretical results exist concerning the stress-free no-AFD $SrTiO_3$, owing to the difference of XC functionals. Here, the experimental results in Fig. 3(a) are under the influence of both AFD rotation and quantum fluctuation that suppress FE, but FE still appears at a small *uniaxial* strain of ~0.0011 [28], which is considered as an experimental upper bound of *biaxial* strain $|u|$ and is far smaller than the critical $|u|$ estimated by LDA and HSEsol. Therefore, the predictions by the PBEsol and HSE

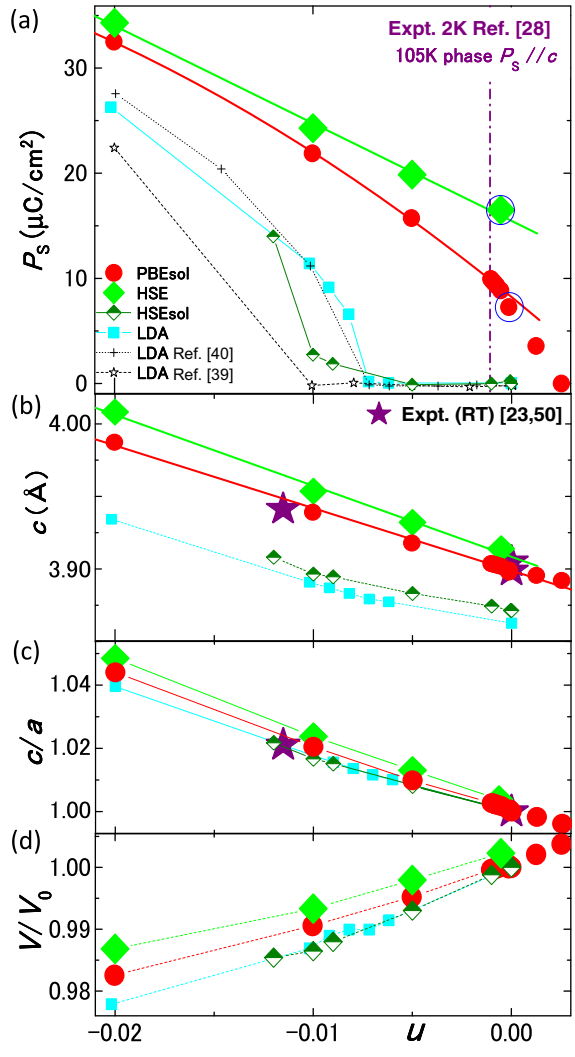

FIG. 3. Strain u dependence of RT phases: (a) $P_S//c$ vs u, (b) c-lattice constant vs u, (c) c/a ratio vs u, and (d) V/V_0 vs u, where V/V_0 is the unit-cell volume normalized by that of the stress-free cubic (O_h^1) phase. In (a), the vertical dash-dotted lines represent experimental critical strain at 2 K below which FE ($P_S//c$) appears by a uniaxial stress along $[1,1,0]_{pc}$ [28]. Filled red circles, filled green diamonds, half-filled dark green diamonds, and light blue squares represent the results of PBEsol, HSE, HSEsol, and LDA, respectively. These LDA results in (a) agree with the previous LDA ones [39–41] shown by open black asterisks [40] and black plus signs [39]. In (b) and (c), filled purple asterisks represent experimental values [23,50]. The red circle and green diamond encircled by blue open circles in (a) represent P_S of the lattice for the minimum free energy under the stress-free condition by PBEsol and HSE, respectively, and are at $u < 0$ because of the spontaneous strain.

calculations should be more appropriate than those by LDA and HSEsol.

This conclusion was supported by the c-lattice constants of PBEsol and HSE in Fig. 3(b) that agree with the experimental ones with and without strain [23,50], whereas those by LDA and HSEsol do not. In Figs. 3(b), all the experimental lattice constants are those at RT, except for one point at $u = 0$, which is of a pseudocubic unit cell at 4 K. The experimental lattice constants for $u < -0.01$ are of thin films at RT, but can be regarded approximately as 0 K data because the strain effect surpasses the effect of 300 K. Such dominance of strain over the temperature effect, i.e., thermal fluctuations, was shown in $BaTiO_3$ [49]. This result [49] is expected to hold for $SrTiO_3$ because the elastic energy at a given u was almost the same for $SrTiO_3$ and $BaTiO_3$, as shown in Sec. VI.

Interestingly, Fig. 3(a) shows that FE also exists for $c/a < 1$, i.e., under tensile stress. In addition, the stress-free orthogonal phase had $P_S//[001]$ and free energy similar to those of the stress-free $\varphi = 0$ tetragonal phase (C_{4v}^1).

The c/a ratio calculated by PBEsol, HSE, HSEsol, and LDA agreed with experimental ones [Fig. 3(c)], despite the mutual disagreements in P_S [Fig. 3(a)]. This shows that the lattice parameters responsible for the different P_S in Fig. 3(a) are mainly the unit-cell volume. This is supported by the comparison of Fig. 3(a) with Fig. 3(d) in which the strain dependence of P_S aligns to that of the unit-cell volume given by each XC functional. These results justify the comparison of the theoretical lattice constants of the O_h^1 phase with the experimental average lattice constant $(a^2c)^{1/3}$ of the D_{4h}^{18} phase in Fig. 2.

V. 105 K PHASES

The experimental ground state of the 105 K phases under no external stress is PE (D_{4h}^{18}), with AFD angle φ under no external stress and φ_0 being ∼1.4° [22] to ∼2.1° [21]. The calculations with PBEsol and HSE yielded $\varphi_0 = 5.25°$ and 1.8°, respectively.

The vertical lines in Fig. 4(a) shows the critical strain for $P_S//[001]$ of the single-crystal experiments at 2 K [28,29]. This critical strain $|u_c|$ is considered as an experimental upper bound of the *biaxial* $|u|$ for $P_S//[001]$, as discussed in Sec. IV.

This *upper bound* of $|u_c| < 0.0011$ agreed with the present calculations with PBEsol in Fig. 4(a), while a more appropriate upper bound of $|u_c|$ appears to be 0.0011/2 (Sec. V). However, quantum fluctuations exist in experiments to suppress FE, whereas these PBEsol calculations are for the 105 K phases under no quantum fluctuations. Therefore, these PBEsol calculations are considered to underestimate FE.

The PBEsol calculations in Fig. 4(b) show that the stress-free minimum free-energy phase is PE (D_{4h}^{18}). On the contrary, the HSE calculations show that the stress-free minimum free-energy phase within $D_{4h}^{18} - C_{4v}^{10}$ is FE with $P_S//[001] = 16\,\mu C/cm^2$; the free energy of this FE phase was lower than that of the PE phase [Fig. 4(b)]. φ and c_{pc} of this FE phase are slightly larger than those of the D_{4h}^{18} PE phase [Figs. 4(c) and 4(d)].

The a- and c-lattice constant and φ_0 of the D_{4h}^{18} PE phase calculated with HSE agreed with the experiments [23,25] much better than those calculated with PBEsol [Figs. 4(c) and 4(d) and Appendix A]. Moreover, PBEsol, which was considered to yield a lower bound of FE, also predicted that the stress-free 105 K phase was FE when it was calculated with the experimental φ_0. All of these results show that the stress-free 105 K phase is FE in the absence of fluctuations and the HSE results are more consistent with the stress experiments [28] than the PBEsol results.

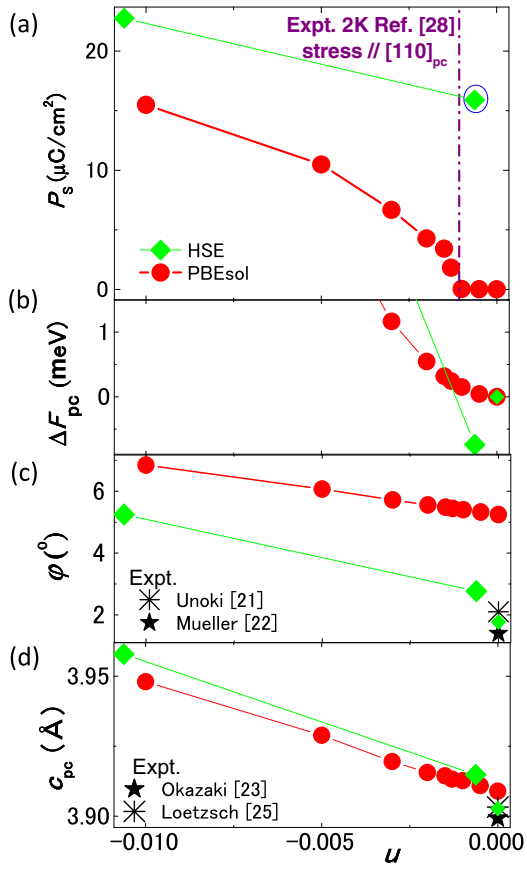

FIG. 4. Strain u dependence (105 K phases) of (a) $P_S//c$. (b) Difference of the free energy per pseudocubic cell from that of stress-free PE phase (D_{4h}^{18}) ΔF_{pc}. (c) AFD rotation angle φ and (d) c-lattice constant. Filled green diamonds and filled red circles represent HSE and PBEsol results, respectively. Small filled green diamond at $u = 0$ in (b)–(d) represents stress-free PE phase (D_{4h}^{18}) calculated with HSE. Vertical dash-dotted lines in (a) represent experimental critical strain at 2 K below which FE ($P_S//c$) appears by a uniaxial stress along $[1, 1, 0]_{pc}$ [28]. The green diamond encircled by a blue open circle in (a) represents P_S for the minimum free energy by HSE under the stress-free condition and is at $u < 0$ because of the spontaneous strain.

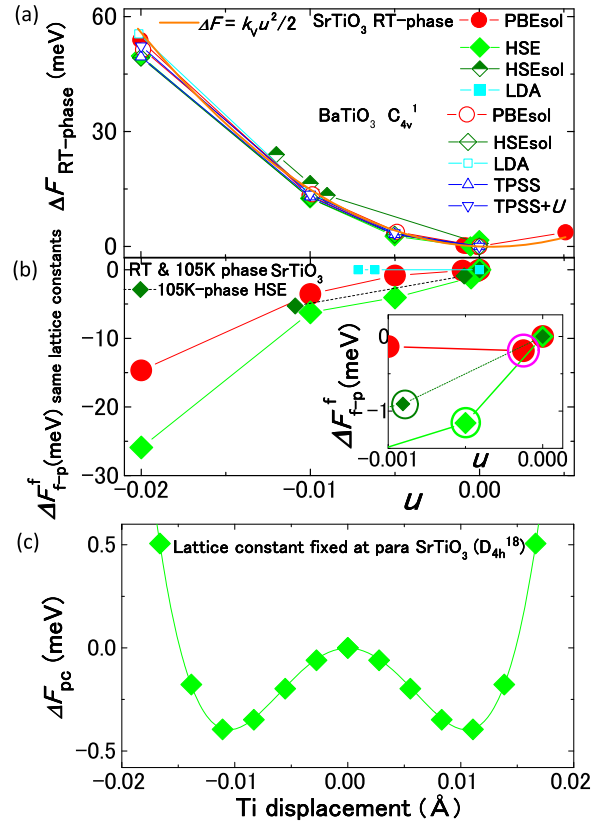

FIG. 5. Analyses of free energy (a) ΔF vs u for the RT-phase $SrTiO_3$ and $BaTiO_3$, where ΔF is the change of free energy from the stress-free O_h^1 PE phase. The orange solid line shows the fitting with $\Delta F = k_v u^2/2$ to the $SrTiO_3$ data. (b) ΔF_{f-p}^f vs u of the RT and the 105 K phase $SrTiO_3$, where ΔF_{f-p}^f is free-energy difference between the FE and PE phases that have the same a and c lattice constants. The meanings of the symbols for $SrTiO_3$ are the same as Fig. 3. For the RT phases, the internal coordinates of the PE phase (D_{4h}^1) at $u < 0$ are the same as those of the O_h^1 PE phase. For the 105 K phases, the internal coordinates of the PE phase (D_{4h}^{18}) at $u < 0$ are the same as those of the stress-free D_{4h}^{18} phase. In an enlarged view in the inset of (b), the stress-free RT phase at the free-energy minimum (C_{4v}^1) calculated with PBEsol and HSE are encircled by a pink and a green open circle, respectively. The stress-free 105 K phase at the free-energy minimum (C_{4v}^{10}) calculated with HSE is encircled by dark green open circles. (c) The difference of free energy per pseudocubic cell from that of the stress-free PE phase (D_{4h}^{18}) ΔF_{pc} vs Ti displacement of the Slater-mode distortion from the PE phase position calculated with HSE for 105 K phase $SrTiO_3$. In these frozen phonon calculations, four Ti's, eight O2's, and four O1's in Fig. 1 are displaced along the z axis with other atoms being fixed at the D_{4h}^{18} positions. The maximum $|\Delta F_{pc}|$ is smaller than $|\Delta F_{f-p}^f|$ of the stress-free condition (∼0.74 meV) in Fig. 5(b) because the lattice constants and φ are fixed at the values of the D_{4h}^{18} PE phase (i.e., not relaxed). The ratio of displacements of Ti, O2, and O1 are 1 : −3.71 : −3.95. Solid lines are fitting to the data.

VI. COMPARISON OF FREE-ENERGY GAIN WITH FLUCTUATION

We have examined FE phases with $P_S//[001]$. The results suggested that the HSE and PBEsol results were appropriate for the RT phases and the HSE results were appropriate for the 105 K phases. This section summarizes the results in Secs. III–V and examines the free energy to consider the effect of fluctuation and the implications of the present results.

A. Accuracy of the results and free-energy gain of FE phase

In Fig. 5(a), the difference of the free energy ΔF from the stress-free state of the RT phase $SrTiO_3$ (O_h^1, D_{4h}^1, C_{4v}^1) and the RT phase $BaTiO_3$ (C_{4v}^1) is on a single curve despite the difference in chemical properties and P_S. This implies that the increase in free energy caused by strain is mostly due to the contraction of the unit-cell volume. Because the *difference in the free energy between the FE and PE* phase ΔF_{f-p}^f in Fig. 5(b) is much smaller than ΔF, the error in the estimation of unit-cell volume as in Fig. 3(d) results in large errors in ΔF_{f-p}^f. Appendix A and Fig. 3 suggest that the errors in HSE were small in both RT and 105 K phases.

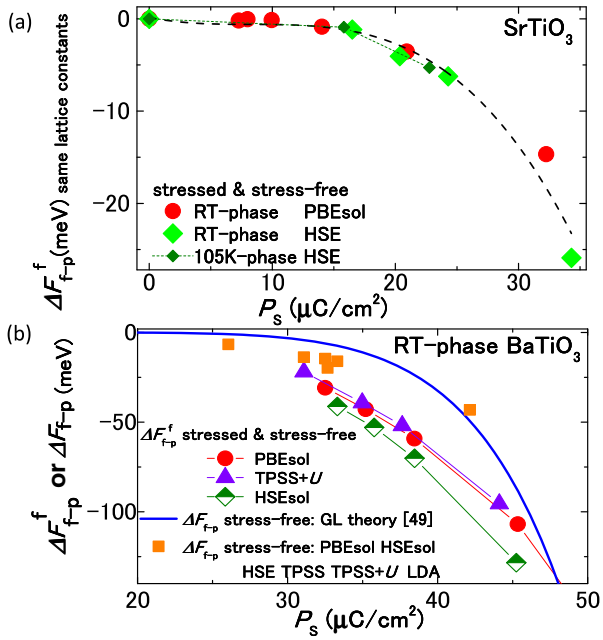

FIG. 6. (a) $\Delta F^{\rm f}_{\rm f-p}$ vs $P_{\rm S}//c$ for $SrTiO_3$, where $\Delta F^{\rm f}_{\rm f-p}$ is the free-energy difference between the FE and PE phases that have mutually the same a- and c-lattice constants. The internal coordinates of the PE phase are the same as those explained in Fig. 5. (b) $\Delta F^{\rm f}_{\rm f-p}$ vs $P_{\rm S}$ for $BaTiO_3$, with $\Delta F_{\rm f-p}$ vs $P_{\rm S}$ calculated with six different XC functionals (orange filled squares), where $\Delta F_{\rm f-p}$ is the free-energy difference between the stress-free FE phase and stress-free PE phase [49]. The blue solid lines show $\Delta F_{\rm f-p}$ by the GL theory for $BaTiO_3$ [49]. In (a) and (b), red filled circles, green filled diamonds, purple filled triangles, and dark-green half-filled diamonds represent PBEsol, HSE, TPSS+U, and HSEsol for $\Delta F^{\rm f}_{\rm f-p}$ of $SrTiO_3$ or RT phase $BaTiO_3$. In (a), small dark-green filled diamonds represent $\Delta F^{\rm f}_{\rm f-p}$ calculated with HSE for 105 K phases. The black dashed lines represent fitting to the data. These results show that $\Delta F^{\rm f}_{\rm f-p}$ is a measure of the energy gain of the FE phase with $P_{\rm S}//c$.

$\Delta F^{\rm f}_{\rm f-p}$ of HSE changed with u more sensitively than $\Delta F^{\rm f}_{\rm f-p}$ of PBEsol in Fig. 5(b). Here, to remove the elastic contribution, $\Delta F^{\rm f}_{\rm f-p}$ is the free-energy difference between the FE phase ($C^1_{4\rm v}$, $C^{10}_{4\rm v}$) and the PE phase ($D^1_{4\rm h}$, $D^{18}_{4\rm h}$) that have the same lattice parameters but for different internal ion positions. The inset of Fig. 5(b) shows that $|\Delta F^{\rm f}_{\rm f-p}|$ for the stress-free state calculated with HSE is much larger than that calculated with PBEsol.

The interpretation that $F^{\rm f}_{\rm f-p}$ is *the energy gain of the FE phase* is supported by Fig. 6(a), showing that $\Delta F^{\rm f}_{\rm f-p}$ is a single function of $P_{\rm S}$. This interpretation is further supported by similar plots for $BaTiO_3$ in Fig. 6(b) that show the difference $\Delta F_{\rm f-p}$ in the free energy between the stress-free PE cubic ($O^1_{\rm h}$) and the stress-free tetragonal ($C^1_{4\rm v}$) FE phase by *ab initio* calculations [49]. Moreover, in Fig. 6(b), $\Delta F^{\rm f}_{\rm f-p}$ of $BaTiO_3$ is consistent with $\Delta F_{\rm f-p}$ of both *ab initio* calculations and the Ginzburg-Landau (GL) theory [49].

To determine the best theoretical estimate of $\Delta F^{\rm f}_{\rm f-p}$, we summarize the accuracy in Secs. III–V. In Figs. 2 and 3(b), the lattice constants of both stress-free and strained RT phases by HSE and PBEsol agreed with experiments. In Fig. 4(d) and Appendix A, the lattice constants of the stress-free 105 K PE phase by HSE agreed with experiments, whereas those by PBEsol and LDA did not. Consistently with $F^{\rm f}_{\rm f-p}$ in Fig. 5(b), φ estimated by HSE changed with u more sensitively around $u = 0$ than PBEsol, which enabled the excellent agreement of φ_0 by HSE with experiments [21,22] [Fig. 4(c)]. Therefore, the estimation of the lattice parameters by HSE is sensitive and accurate, which is consistent with the studies of polaron [64]. In addition, Sec. V also showed that the HSE results were consistent with experiments [28] and the PBEsol results were not. Here, HSE predicted that the stress-free 105 K phase was FE at the minimum free energy, and, with the use of the experimental φ_0, PBEsol yielded the same prediction. In addition, the free energy calculated against the Slater mode also supported that free energy of the stress-free FE phase ($C^{10}_{4\rm v}$) was lower than that of the stress-free PE phase ($D^{18}_{4\rm h}$) [Fig. 5(c)].

The stringent accuracy requirements on the lattice constants and φ are shown for the estimation of FE of $SrTiO_3$ [42,43,45]. Therefore, in our opinion, it is conclusively proven that in the absence of fluctuations, the stress-free 105 K phases ($D^{18}_{4\rm h}$, $C^{10}_{4\rm v}$) at the free-energy minimum are FE. The estimate of $\Delta F^{\rm f}_{\rm f-p}$ of the RT and 105 K phases by HSE should also be reliable. In our opinion, it is also conclusively proven that in the absence of fluctuations, the stress-free RT phase at the free-energy minimum is FE (Table I). This is because it was shown by both PBEsol and HSE in Sec. IV, where PBEsol was accurate or slightly underestimated FE of the RT phases and HSE was accurate or slightly overestimated FE of the RT phases (Fig. 2).

The inset of Fig. 5 shows that the free-energy gain of the RT FE phase ($C^1_{4\rm v}$) and 105 K FE phase ($C^{10}_{4\rm v}$) $|\Delta F^{\rm f}_{\rm f-p}|$ is 1.66 and 0.74 meV per pseudocubic cell (HSE), respectively. The comparison of $c_{\rm pc}$ of the stress-free FE phase ($u = -0.0006$) and PE phase ($u = 0$) in Fig. 4(d) indicates that the contraction of $c_{\rm pc}$ by 0.012 Å is sufficient to suppress the 105 K FE. Therefore, not only optical phonons but also acoustic phonons coupled with optical phonons can suppress FE. The energy for this contraction $\Delta c_{\rm pc}$ is $k(\Delta c_{\rm pc})^2/2 = 0.77$ meV per pseudocubic unit cell with use of $k = 170\,{\rm N/m}$. This value is consistent with the above $|\Delta F^{\rm f}_{\rm f-p}| = 0.74$ meV and was estimated in the following manner: the fitting $\Delta F = k_{\rm v}u^2/2$ to the plots in Fig. 5(a) yields $k_{\rm v} = 260\,{\rm N/m}$, and Fig. 3(d) shows $\Delta V/V \approx 2u - \lambda u \approx 1.5u$, where λ is the Poisson ratio, i.e., $k_{\rm v} \approx 1.5k$.

The present conclusions are quantitatively consistent with phonon dynamics calculations [65] showing that the ground state of the RT phase is FE and $\Delta F^{\rm f}_{\rm f-p} \sim 1 - 2$ meV per cubic cell.

B. Estimation of quantum fluctuation

Müller and Burkard [2] examined the postulate of Kurtz [66] for the *homogeneous* suppression of FE by quantum fluctuations $\Delta z < \Delta\zeta$, where Δz and $\Delta\zeta$ are the FE displacement and the mean quantum mechanical amplitude (0.077 Å [2]), respectively. $\Delta z = c_{\rm pc}\Delta z_{\rm Ti-O2}$ is 3.91 Å × 0.0175 = 0.069 Å (HSE) or 3.91 Å × 0.0060 = 0.023 Å (PBEsol with φ fixed at 2.26° ≈ experimental φ_0) for the stress-free 105 K phase shown in Appendices A and B, and Figs. 7(b) and 9.

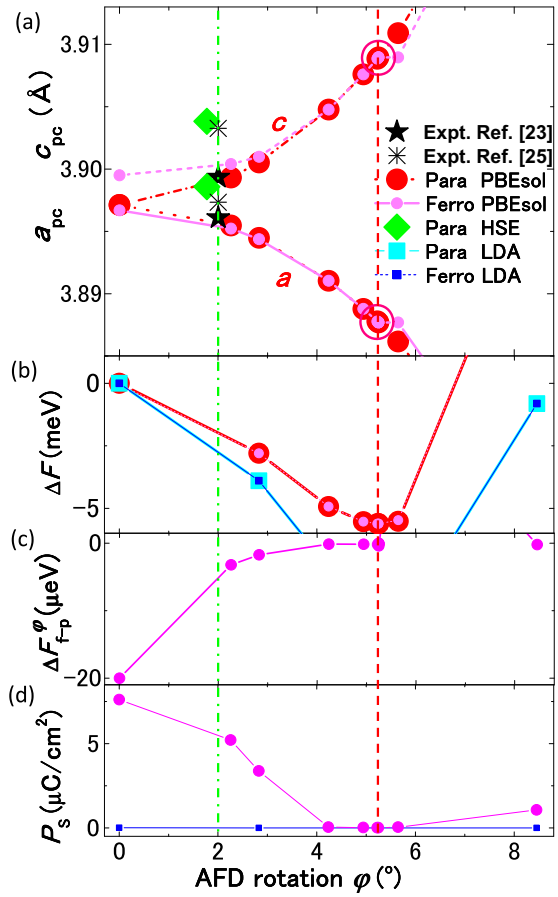

FIG. 7. AFD rotation angle φ dependence (105 K phases) of (a) a- and c-lattice constant, (b) ΔF (change of free energy from the PE phase at $\varphi = 0$), (c) difference of free energy between PE and FE phases with $P_S//c$ at the same φ (ΔF_{f-p}), and (d) P_S. Large red and small pink filled circles represent the PE and FE phases ($P_S//c$) calculated with PBEsol, respectively. Filled green diamonds in (a) represent the PE phase calculated with HSE. Large light-blue and small blue filled squares in (b) and (d) represent the PE and FE phases ($P_S//c$) calculated with LDA, respectively. Asterisks represent experiments [23,25]. The red dashed and the green dash-dotted vertical lines show φ at the minimum ΔF by PBEsol and the experimental φ, respectively. The lattice constants at the free-energy minimum by PBEsol are encircled by red open circles in (a) and are much more different from experimental ones than those given by HSE. The lattice constants by LDA are outside of the range of the plot of (a).

Therefore, "$\Delta z < \Delta\zeta$" is satisfied and the quantum fluctuation is considered to suppress the *long-range order* of FE.

In addition, the energy scale E_{QM} of the quantum fluctuation is estimated from the temperature of the crossover T_{cr} from the thermal to the quantum fluctuation: We assume $E_{QM} = E_{TH}$ at $T_{cr} \approx 4$ K, where E_{TH} is the energy scale of the thermal fluctuation and T_{cr} is estimated from the temperature (T) dependence of permittivity [2]. $E_{TH} = (5-1) \times 3k_B T_{cr}/2 \approx 2$ meV at T_{cr}, and we obtain $E_{QM} \approx 2$ meV per pseudocubic unit cell. Because $E_{QM} \gg |\Delta F^{f}_{f-p}|$ (0.74 meV), this approach shows again that the quantum fluctuation is considered to suppress the *long-range order* of FE. It is obvious from these arguments that the thermal fluctuations at RT completely suppress FE including those of RT phases.

C. Examinations of effect of fluctuations

We examine the appropriateness of the above criteria "$E_{FL} \gg |\Delta F^{f}_{f-p}|$" for the suppression of FE, where E_{FL} is the energy scale of the fluctuation, i.e., $E_{FL} = E_{QM}$ or E_{TH}. The energy gain of FE in tetragonal $BaTiO_3$ $|\Delta F^{f}_{f-pBTO}|$ is 15–10 meV per five-atom unit cell [Fig. 6(b)], and the experimental Curie temperature T_C for the FE-PE phase transition is approximately 400 K. Therefore, E_{FL} at T_C is $6k_B T_C = 200$ meV and is ten times larger than $|\Delta F^{f}_{f-pBTO}|$.

In addition, the energy gain of the transition from the RT PE phase (O^1_h) to the 105 K PE phase (D^{18}_{4h}) $SrTiO_3$ calculated with PBEsol was 6 meV per pseudocubic unit cell in Appendix A. This value is eight times smaller than E_{FL} at 105 K ($6k_B T = 50$ meV).

These examinations indicate that a well-defined transition to a higher-symmetry phase takes place for approximately $E_{FL} > 10\,|\Delta F^{f}_{f-p}|$. The preceding arguments showed that this condition was marginally satisfied by E_{QM} and $|\Delta F^{f}_{f-p}|$ of the 105 K phases. That is, at least, a long-range order of FE of the 105 K phase appears marginally suppressed by quantum fluctuations. This conclusion is consistent with the experimental paraelectricity and incipient FE [3,28–31].

The energy gain of FE $|\Delta F^{f}_{f-p}|$ (>20 meV) calculated for $u \leqslant -0.02$ with HSE in Figs. 5(b) and 6(a) satisfies both $|\Delta F^{f}_{f-p}| \gg E_{QM}$ and $|\Delta F^{f}_{f-p}| > E_{TH}$ for <30 K. Therefore, FE with $P_S//[001]$ can exist at <∼40–50 K for $u < -0.02$. This inference is supported by the criterion for the quantum PE [2,66]: the FE displacement $\Delta z >$ mean quantum mechanical amplitude $\Delta\zeta = 0.077$ (Sec. VI B); $\Delta z_{Ti-O2} = 0.097$ Å ($\Delta z_{O2} \sim 0.09$ Å) already at $u = -0.01$ (HSE), where Δz_{Ti-O2} and Δz_{O2} are the distance between Ti and O2 and the displacement of O2 from the PE phase position, respectively. In addition, the HSE results for the 105 K phases in Fig. 5(b) indicate that $|\Delta F^{f}_{f-p}| \approx E_{QM}$ at $u = -0.003$. Therefore, the FE phase would exist for $u < -0.003$ in the presence of quantum fluctuations, which approximately explains the experiments [28–30].

D. Paraelectricity by fluctuation

In this section, we concentrate on the ground state of $SrTiO_3$ and, therefore, the 105 K phase. Müller and Burkard [2] analyzed the origin of the T-independent permittivity at low T and wrote "The dipolar ferroelectric interaction is, on the other hand, certainly involved." That is, they concluded the existence of dipoles in the T-independent permittivity state, i.e., quantum PE state of $SrTiO_3$. This existence of the dipoles is equivalent to that of short-range polar phases in the quantum PE phase.

Such nanoscopic polar phases are expected to become coherent by impurities and strain. Therefore, the existence of these phases is consistent with the experimental observations of FE by a tiny amount of impurity, e.g., 0.002 mol [3,31], and its precursory phenomenon: a FMR [34–38] that can be regarded as a sort of PNR [67] found in relaxors.

When dipoles are dominant in the PE phase, the FE-PE phase transition is called the *order-disorder* transition as

opposed to displacive transition. Many FE phase transitions including those of typical perovskite oxides are known mixtures of order-disorder and displacive type. For example, an order-disorder-type FE phase transition, i.e., polar structures in a PE phase that coexist with a displacive transition, is experimentally shown in $BaTiO_3$ through birefringence [68] and nuclear magnetic resonance (NMR) [69]. Müller [70] pointed out the order-disorder component in the 105 K transition of $SrTiO_3$ based on the studies of electron paramagnetic resonance (EPR) and neutron scattering [71]. These results are consistent with our conclusions presented above.

Two PE states can be considered to exist when the PE phase originates from the suppression of FE: (1) *homogeneous PE phase* discussed in Ref. [2] and (2) inhomogeneous PE phase. The arguments in Sec. VI A indicate that the contraction and elongation of the c axis (c_{pc}) suppresses and enhances FE, respectively, and therefore the spatial and temporal oscillation of phonons should yield regions or periods of reduced and enhanced FE. Therefore, the PE state of $SrTiO_3$ may be inhomogeneous in the deep nanometer scale in a short-time interval of phonon frequency.

In this case, "how a polar or nano-FE phase exists in the presence of quantum fluctuation" requires a large cell calculation consisting of many unit cells. This state may be a mixture of temporal nanoscale FE and PE phases, or an assembly of domains [72,73]. The latter case was theoretically proposed for the cubic phase of $BaTiO_3$ [72] and was supported by *ab initio* molecular dynamics [73]. These models proposed that the net P_S is zero when averaged over in a region much larger than the unit cell, which explains the experimental observation of the PE phase of $SrTiO_3$.

E. Conductivity at $LaAlO_3/SrTiO_3$ and its domain boundaries

GL theories [17,18] using the metal-insulator-semiconductor (MIS) theory [74] and the Ando-Fowler-Stern theory for two-dimensional (2D) electrons [75] predicted universal existence of the conduction layer at polar discontinuity such as insulator/FE and charged domain boundaries. This prediction for the conduction layer at insulator/FE was verified by *ab initio* calculations [76] and experiments [18], and the conduction layer at charged domain boundaries is reported by many recent experiments.

Figures 4(a) and 5(b) show that strain $u \leqslant -0.02$ firmly stabilizes FE of $SrTiO_3$ and yields a substantial P_S comparable with P_S of $BaTiO_3$, where u exerted by a perfect epitaxy of $LaAlO_3$ on $SrTiO_3$ is -0.03. That is, $LaAlO_3/SrTiO_3$ (LAO/STO) at low T is regarded as an insulator/FE phase having polar discontinuity. Actually, the "polar state" of the $SrTiO_3$ surface at LAO/STO was confirmed by second harmonic generation (SHG) by Savoia *et al.* [11] and Günter *et al.* [10] (Appendix C), and was called "polar catastrophe." Because the "polar state" of $SrTiO_3$ is identical with the FE of $SrTiO_3$, the theories [17,18] indicate that the existence of 2D electrons at the surface of LAO/STO interface and the predicted thickness of the layer $\approx$2 nm [18] agree with the experimental values.

However, 2D electrons at LAO/STO should be more complex because it shows no hole layer as opposed to the predictions of the theories [17,18]. Actually, we observed experimentally that the heating of $BaTiO_3$ above 200 °C in vacuum generated a surface conduction layer owing to oxygen (O) vacancy. In all the experiments of LAO/STO, $LaAlO_3$ is deposited at >400 °C in vacuum, and serious O-vacancy formation that is unrecoverable by postannealing is expected. Moreover, Iglesias [9] showed theoretically that the O-vacancy formation is enhanced by strain, which is exerted by the $LaAlO_3$ layer. In addition, the intermixing of a few atomic layers at LAO/STO is expected, which is unavoidable in vacuum deposition.

These O vacancies and the intermixing at LAO/STO were experimentally confirmed by Pauli *et al.* [13] and Siemons *et al.* [14]. Both O vacancy and La are electron donors for $SrTiO_3$ [77–80]. Therefore, the experimental observation of the conductance at LAO/STO is substantially due to O vacancy and La, where a modulation doping mechanism [81] may assist it further.

Consequently, the origin of 2D electrons at LAO/STO is summarized as the cooperation of the chemical doping of O vacancy and La *assisted by polar discontinuity* [17,18], which explains the absence of hole conductance. The original polar catastrophe is unique to the atomic-layer sequence of $LaAlO_3$, which is unphysically oversensitive to environments and different from the above polar state of $SrTiO_3$. When we identify the polar state as FE, the present explanation agrees with that by Mannhart [82] (Appendix C).

This explanation is supported by the existence of 2D-electron conductance in various oxide/$SrTiO_3$, where $SrTiO_3$ is a single crystal. In particular, the free surface of $SrTiO_3$ single crystals having O vacancy created by Ar bombardments also showed 2D-electron conductance [83,84]. Furthermore, the interfaces of $SrTiO_3$ single crystals with the Al_2O_3 layer and amorphous oxide layer also show 2D-electron conductance [85–87]. In particular, the interface of a $SrTiO_3$ single crystal with an *amorphous* $SrTiO_3$ film also shows 2D-electron conductance [85]. In these 2D electrons [83–87], no original polar catastrophe exists, but the O vacancy and polar discontinuity are expected to exist owing to the strain- and symmetry-constriction-induced FE (Appendix C). In addition, for a large strain, domain formation is expected, which explains the inhomogeneous conduction [12] as a contribution of domain boundary conduction [18].

VII. SUMMARY

In the absence of thermal and quantum fluctuations, some *ab initio* calculations showed that stress-free stoichiometric $SrTiO_3$ at the free-energy minimum was paraelectric (PE) [39–41], while the others [42–45] showed the instability of the PE phase. Consequently, the properties of a possible ferroelectric (FE) phase of $SrTiO_3$ such as lattice parameters, P_S, and free energy have been unknown. The present paper showed the existence of a stress-free FE phase at the energy minimum in the absence of thermal and quantum fluctuations, revealing the properties of the RT and 105 K FE phases under a stress-free and biaxially strained condition (Table I).

For this, we used a fourfold approaches: (1) use of the XC functional (HSE) that yielded the best agreement of theoretical lattice parameters of $SrTiO_3$ with experimental ones,

(2) use of PBEsol for a good lower bound of ferroelectricity (FE), (3) consistency with strain effect, where the experimental data are available [28–30,50], and (4) use of the AFD angle dependence of FE. Here, the increase of P_S of tetragonal FE phases by compressive in-plane stress is mathematically self-evident [17,49], being established since the proposal of the GL theory by Devonshire in 1949 [28–30,50,88,89].

The essentialness of the accuracy of lattice parameters for FE has been shown by the *ab initio* studies of FE [39–43,45–49]. The lattice constants of the stress-free RT PE phase $SrTiO_3$ (O_h^1) calculated with PBEsol and HSE agreed with the experimental values [23–25] better than the experimental variation (Fig. 2) [23–25,50]. Both PBEsol and HSE predicted that in the stress-free condition, the FE phase (C_{4v}^1) had a lower free energy than the PE phase (O_h^1) and a substantial $P_S \sim 7 - 16\,\mu C/cm^2$ (Sec. IV).

The lattice parameters of the stress-free 105 K PE phase (D_{4h}^{18}) calculated with HSE agreed excellently with the experimental ones [23–25] (Sec. V). The comparison with the experiments [28] [Fig. 4(a)] supported that HSE was also accurate for the 105 K phases. In addition, Sec. VI and Appendix A supported that the HSE results were accurate, showing that PBEsol gave a good lower bound of FE.

For 105 K phases, HSE predicted that the FE phase (C_{4v}^{10}) had the lower free energy than the PE phase (D_{4h}^{18}), possessing a substantial $P_S \sim 16\,\mu C/cm^2$ in the stress-free condition, which was also shown by PBEsol when φ_0 was fixed at the experimental value (Appendix A). The theoretical c- and a-lattice parameters of this FE phase were 0.3% longer and 0.06% shorter that those of the PE phase (D_{4h}^{18}), respectively, and the theoretical φ_0 was 1° larger than that of the PE phase (HSE). In summary, the present study shows that both RT and 105 K stress-free phases of $SrTiO_3$ are FE in the absence of quantum and thermal fluctuations, contrary to previous works [39–41].

These results were examined by considering the thermal and quantum fluctuations in Sec. VI. The energy scales of the thermal fluctuations at RT far exceed the energy gain for the FE phase $|\Delta F_{f-p}^f|$, showing that stress-free $SrTiO_3$ is PE at RT, which is consistent with experiments. Similarly, the stress-free 105 K phase near 0 K was concluded to be a homogeneous [2,66] or inhomogeneous PE phase (D_{4h}^{18}), which is consistent with experiments. This appears to align with the experimental incipient FE.

As a candidate of this inhomogeneous paraelectricity, an assembly of short-range FE phases formed by fluctuation is proposed in Sec. VI D. In this context, an order-disorder component exists in the quantum PE state of $SrTiO_3$ [2,70,71]. We expect that the defects and impurities yield local stresses and suppress quantum fluctuations, which enables a prompt emergence of FE by tiny stimulation such as defects [3,28–31] and explains FMR [34–38].

For the in-plane biaxial strain $u < -0.02$, $P_S//[001]$ is considered to exist even in the presence of quantum and thermal fluctuations at ~40–50 K in Sec. VI C. This prediction appears consistent with the experiments for FE-like properties at RT found at the surface and in nanodots [15,16], when defect-induced strain is assumed. Therefore, the 2D electrons at the $LaAlO_3/SrTiO_3$ interface [10–14] were considered to be due to the cooperation of the chemical doping of O vacancy and La and polar discontinuity [17,18] (Sec. VI E and Appendix C).

The comparison of P_S in Figs. 3 and 4 reveals a marked difference between P_S of the C_{4v}^1 phase and P_S of the C_{4v}^{10} phase *at the same strain u*, showing the substantial effect of φ or symmetry. Although the mechanical effects of epitaxy have conventionally been represented by u, the epitaxy or deposited thin film also constrains symmetry, which has been missing in the macroscopic treatment of the epitaxial effects. Here, ΔF_{f-p}^f of the stress-free RT and 105 KFE phase calculated with HSE were 1.66 and 0.74 meV, respectively [Fig. 5(b)]. This difference is due to the disparity between C_{4v}^1 and C_{4v}^{10} symmetry. In most experiments, the epitaxy of $SrTiO_3$ and many FE phases stabilizes the C_{4v}^1 symmetry, and therefore P_S should be stabilized by both the strain and symmetry constraints. The latter can be called *enhancement of FE due to symmetry constriction*. Examples of this mechanism in LAO/STO are discussed in Appendix C.

PBEsol is currently a standard XC functional for solids and was accurate for both the RT and 105 K phases for large compressive strain ($|u| > 1\%$), e.g., yielding $P_S > 15\,\mu C/cm^2$ and φ similar to those of HSE (Figs. 3, 4, and 7). Therefore, PBEsol can be a substitute of HSE for $SrTiO_3$ for $u < -1\%$, although it underestimates the stability of the FE phase [Fig. 5(b)].

ACKNOWLEDGMENTS

The author acknowledges enlightening discussions with Dr. Jochen Mannhart, Dr. Yuji Tsujimi, Dr. Hiromoto Uwe, Dr. Masao Arai, and Dr. David Vanderbilt.

APPENDIX A: φ DEPENDENCE OF 105 K PHASE

This section summarizes the φ dependence of the 105 K phase calculated with PBEsol and LDA, while P_S is along [001]. The φ dependence of the c-lattice constant in Fig. 7(a) is consistent with the strain dependence of φ and c_{pc} in Figs. 4(c) and 4(d). This also holds for the a-lattice constant because $a = a_0(1 + u)$.

Unless otherwise stated, all the results below are given by PBEsol, shown by red filled circled in Fig. 7. In Fig. 7(a), the experimental a- and c-lattice constants [23,25] are plotted at the experimental $\varphi_0 = 2°$, where the PE phase at $\varphi = 0$ is identical to the RT PE phase (O_h^1). The a- and c-lattice constants of the PE phase at $\varphi_0 = 2°$ by PBEsol agree with the experiments [23,25] within ~0.013–0.045% and ~0.001–0.1%, respectively. However, in Fig. 7(b), the free energy ΔF reached the minimum at $\varphi = 5.2°$. At $\varphi = 5.2°$, the discrepancy between the experimental and theoretical lattice constants amounts to 0.2%. This discrepancy is far larger than that given by the HSE calculations as below.

Figures 7(a) and 7(b) shows that both theoretical lattice constants and free energy F are determined mainly by the AFD angle φ. Therefore, the deviation of the lattice constants calculated from the experimental ones is mainly due to the overestimation of φ_0. Consequently, PBEsol underestimates the energy gain $|\Delta F_{f-p}{}^{\varphi}|$ from a PE phase to a FE phase and P_S substantially [Figs. 7(c) and 7(d)]. $|\Delta F_{f-p}{}^{\varphi}|$ decreased with φ , having negligible values, i.e., $< 1\,\mu eV$ for $4° < \varphi < 8°$.

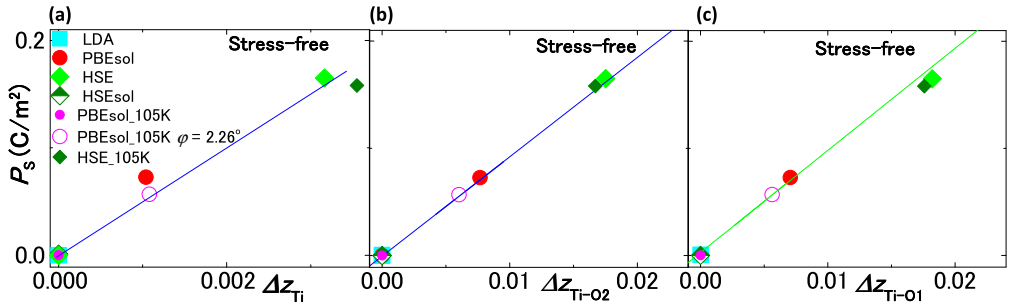

FIG. 8. Correlation of P_S with atomic displacements (a) Δz_{Ti}, (b) Δz_{Ti-O2}, and (c) Δz_{Ti-O1} in stress-free RT and 105 K phase $SrTiO_3$. Sr atom is at (0, 0, 0). The displacements of Ti, O1, and O2 (Δz_{Ti}, Δz_{O1}, and Δz_{O2}) are measured from the PE phase (O_h^1, D_{4h}^{18}) position of each ion along the c axes (z axis) in fractions of the c-lattice constant of a cubic or a pseudocubic unit cell, i.e., $c = 1$. O1 and O2 are defined in Fig. 1(b). Δz_{Ti-O2} and Δz_{Ti-O1} are the differences between Δz_{Ti} and Δz_{O2} and between Δz_{Ti} and Δz_{O1}, respectively. Filled light-blue squares, filled red circles, filled green diamonds, half-filled dark-green diamonds, small filled purple circles, and small filled dark-green diamonds represent the results of LDA, PBEsol, HSE, and HSEsol for the RT phase, and PBEsol and HSE for the 105 K phase, respectively. The open purple circle represents the PBEsol results for the 105 K phase with the AFD angle fixed at 2.26°. The straight lines are a guide to the eye.

In Fig. 7(d), P_S decreased with φ , consistently with $\Delta F_{f-p}{}^{\varphi}$ in Fig. 7(c). At the minimum F, i.e., at $j = 5.2°$, P_S is nearly zero. However, at the experimental $\varphi(\varphi_0 = 2°)$, $\Delta F_{f-p}{}^{\varphi}$ is evidently negative with $P_S > 6\,\mu C/m^2$. This value of P_S is almost comparable with those of the common FE phases.

The slight increase of the energy gain of the FE phase $|\Delta F_{f-p}{}^{\varphi}|$ at $\varphi > 8°$ can be explained by the c_{pc} elongation shown in the strain dependence of c_{pc} in Fig. 4(d). However, these structures have much higher free energy than that of the stress-free ground state, as shown in Fig. 7(b). Therefore, it can only be stabilized by compressive in-plane strain, as shown in Fig. 4(c). Results qualitatively similar to the PBEsol results in Figs. 7(a) and 7(b) were calculated with LDA, but P_S by LDA is zero for all φ [Fig. 7(d)].

If we consider the mixing of phases with different φ_0 by quantum fluctuation [90], the average φ is approximately $3.5° - 4°$. The lattice constants at these φ 's still disagree with experimental values in Fig. 7(a), and P_S is zero, according to Fig. 7(d).

These issues were solved with HSE. The AFD angle at the minimum F (φ_0) calculated with HSE is 1.77°, agreeing with experiments [21,22]. In Fig. 7(a), the HSE a- and c-lattice constants of the D_{4h}^{18} PE phase at $\varphi_0 \sim 1.77°$ are only ~0.032–0.064% and ~0.015–0.12% larger than experiments [23,25], respectively, agreeing with the experimental ones far better than the PBEsol lattice constants at the PBEsol minimum ΔF. Therefore, HSE is considered to yield structure parameters consistent with experiments and be an appropriate XC functional for $SrTiO_3$.

Consequently, HSE was the most accurate for the 105 K phase $SrTiO_3$ among the examined XC functional, whereas PBEsol overestimated φ_0 and underestimated P_S. In addition, Sec. VI showed that the insensitivity of PBEsol to the internal parameters, as suggested in previous reports [49,64].

APPENDIX B: FERROELECTRIC DISTORTIONS AND CHARGE DISTRIBUTIONS

The XC-functional dependence of FE distortions and the electronic charge distributions in the RT and 105 K phases is shown in Figs. 8 and 9, respectively. Theoretical P_S and FE distortions (Δz_{Ti}, Δz_{Ti-O2}, and Δz_{Ti-O1}) depend on the XC functionals shown in Fig. 8. Nonetheless, the plots of P_S vs Δz_{Ti-O2} lie on a single straight line, which is consistent with the results for $BaTiO_3$ [49] and general relationships [91].

In Fig. 8, the values of Δz_{Ti-O2} are ten times larger than those of Δz_{Ti}. Therefore, oxygen atoms, especially O2, are

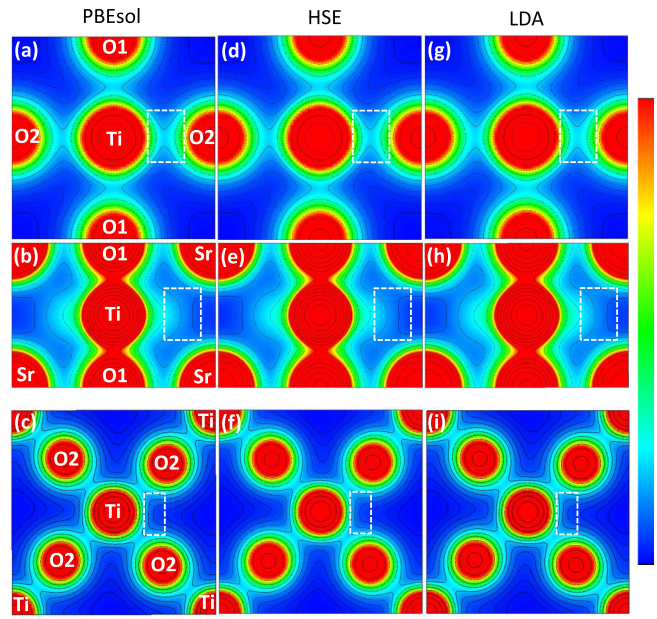

FIG. 9. Distribution of valence charge density ρ of PE phase $SrTiO_3$ calculated *ab initio* with (a)–(c) PBEsol, (d)–(f) HSE, and (g)–(i) LDA. The first and second rows [(a),(d),(g),(b),(e), and (h)] show the RT PE phase (O_h^1), and the third row [(c),(f), and (i)] shows the 105 K PE phase (D_{4h}^{18}). The first and third rows show ρ in the [100] plane, and the second row shows ρ in the [110] plane. The right bar shows the color code, where ρ increases from blue to red. The red color represents $\rho > 0.5e/Å^3$ in the [100] planes [(a), (d),(g), (c),(f), and (i)] and $\rho > 0.1\,e/Å^3$ in the [110] planes [(b),(e), and (h)]. O1 and O2 are oxygen in the TiO2 and SrO layers, respectively [Fig. 1(b)]. The open dashed white squares show the area where the difference between the XC functional is clearly visible.

considered as the main contributor to P_S, which is consistent with the phonon dynamics theory [92]. Because P_S depends linearly on Δz_{Ti}, Δz_{Ti-O2}, and Δz_{Ti-O1} in Fig. 8, the Born charges estimated by different XC functionals are considered almost the same.

The c-lattice constant by HSE increased more rapidly with u than that by PBEsol in Figs. 3(c) and 4(d). In Fig. 3(d), this resulted in the smallest decrease of the unit-cell volume by HSE with u [Fig. 3(d)]. These results suggest that the repulsion force by HSE is larger, i.e., more sensitive than other XC functionals. This may be the reason why in Fig. 8 the FE distortions by HSE were much larger than those by PBEsol, which was consistent with P_S in Figs. 3(a) and 4(a).

The charge density profiles in Fig. 9 show that the charge density ρ by HSE is more confined and depends more on directions than PBEsol and LDA. This is probably one of the reasons that HSE estimated φ and the FE of the 105 K phases more accurately than PBEsol and LDA.

For example, this can be confirmed by the comparisons of the charge density profiles in the open dashed white squares. The comparison of these marked areas in Figs. 9(a), 9(d), and 9(g) shows that a high-ρ region (light blue) is narrower in Fig. 9(d) (HSE) than the others. Similarly, the comparison of the marked areas in Figs. 9(b), 9(e), and 9(h) shows that a low-ρ region (dark blue) is wider in Fig. 9(e) (HSE) than the others. The comparison of the marked areas in Figs. 9(c), 9(f), and 9(i) shows that a low-ρ region (dark blue) is slightly wider in Fig. 9(f) (HSE) than the others.

APPENDIX C: STRAIN- AND SYMMETRY-CONSTRICTION-INDUCED P_S AT LAO/STO

The conductance due to oxygen vacancies and La doping should exist generally at $LaAlO_3/ABO_3$ oxides (A: alkaline earth; B: Ti, Zr, Hf; O: oxygen). The unique properties of $SrTiO_3$ among the ABO_3's are the high electron mobility of single crystals [77] comparable with that of Si $\sim 10^4$ cm^2/Vs at low T and the incipient FE.

In the studies of FE, SHG is a standard tool to detect FE [36,93]. To be exact, the detection of a SHG signal proves the absence of the inversion symmetry. Here, the absence of the inversion symmetry in $SrTiO_3$ is equivalent with the presence of local polarization. In this view, the SHG from $SrTiO_3$ at LAO/STO [10,11] means the existence of polarization in $SrTiO_3$ at LAO/STO (Sec. VI E). The observation of SHG from the *free surface* of $SrTiO_3$ [11] also supports this interpretation because the free surface of $SrTiO_3$ is polar owing to oxygen buckling [94,95].

The existence of strain-induced P_S in LAO/STO in Sec. VI E is directly supported quantitatively by the transmission electron microscopy observations [96]. The maximum c-lattice constant (∼0.4 nm) near the LAO/STO interface in Lee *et al.* [96] corresponds to the c-lattice constant at $u \approx -0.02$ in Fig. 3(b), which implies $P_S \sim 25 - 30\,\mu$C/cm^2 at 0 K according to Fig. 3(a). The same P_S value is obtained from the atomic displacements of Lee *et al.* [96] through the formula in Ref. [91]. Considering the reduction of P_S at RT, these theoretical P_S at 0 K values agree with the experimental P_S at RT estimated by Lee *et al.* [96], supporting both the role of P_S in LAO/STO and the correctness of the present calculations under strain (Figs. 3 and 4).

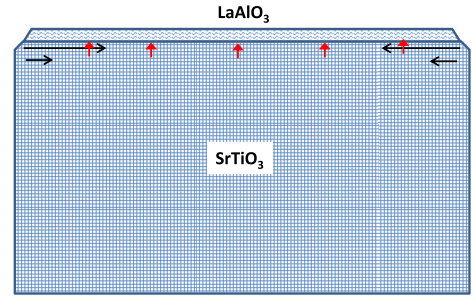

FIG. 10. Schematic explanation of strain-induced P_S in the strained $SrTiO_3$ surface due to the atomically thin $LaAlO_3$ layer. Horizontal black and vertical red arrows show the compressive strain and P_S, respectively.

The strain in the $SrTiO_3$ single crystal induced by a few atomic layers of $LaAlO_3$ might appear unphysical. However, in general, epitaxial strains concentrate only at the interface [96] (Fig. 10) as evidenced in the thickness dependence of the c-lattice constants of epitaxially strained films [97], while the bulk parts are little affected. Therefore, a few atomic $LaAlO_3$ layers can exert strain on a few surface layers of bulk $SrTiO_3$, and the effect of the $LaAlO_3$ thickness is not expected to much increase beyond a certain thickness. Nonetheless, the $LaAlO_3$ should be sufficiently thicker than a unit cell to exert strain $u < -0.0011$ [cf. Fig. 3(a)] to resist the quantum fluctuations.

In addition, the atom positions of thin films are fixed at those during the deposition. Therefore, the thin films should freeze the symmetry of the substrate surface at the deposition temperature. In the case of a thin-film deposition on $SrTiO_3$, the thin film acts to retain the in-plane symmetry of the $SrTiO_3$ surface without AFD ($\varphi = 0$) because $\varphi = 0$ at the deposition temperature. That is, it suppresses C_{4v}^{10} and favors C_{4v}^{1}. This should enhance P_S of $SrTiO_3$, according to the "enhancement of FE due to symmetry constriction" (Sec. VII); in Figs. 3(a), 4(a), and 5(b), P_S of $C_{4v}^{1} > P_S$ of C_{4v}^{10} and $|\Delta F_{f-p}^{f}|$ of $C_{4v}^{1} > |\Delta F_{f-p}^{f}|$ of C_{4v}^{10}. This mechanism works with any thin films, e.g., amorphous films, when they are hard materials such as metal oxides and are deposited above RT. Therefore, this mechanism may be working in not only LAO/STO but also $AlO_x/SrTiO_3$ and amorphous/$SrTiO_3$ [85–87]. Defects, which are electron donors, may also exert strain and constrict symmetry to enhance P_S in Refs. [83,84].

[1] J. H. Barrett, Phys. Rev. **86**, 118 (1952).
[2] K. A. Müller and H. Burkard, Phys. Rev. B **19**, 3593 (1979).
[3] J. G. Bednorz and K. A. Müller, Phys. Rev. Lett. **52**, 2289 (1984).
[4] R. G. Carr and G. A. Somorjai, Nature (London) **290**, 576 (1981).
[5] J. Hwang, R. R. Rao, L. Giordano, Y. Katayama, Y. Yu, and Y. Shao-Horn, Science **358**, 751 (2017).

[6] E. K. H. Salje, O. Aktas, M. A. Carpenter, V. V. Laguta, and J. F. Scott, Phys. Rev. Lett. **111**, 247603 (2013).
[7] H. J. Harsan Ma *et al.*, Phys. Rev. Lett. **116**, 257601 (2016).
[8] M. Honig *et al.*, Nat. Mater. **12**, 1112 (2013).
[9] L. Iglesias, A. Sarantopoulos, C. Magén, and F. Rivadulla, Phys. Rev. B **95**, 165138 (2017).
[10] T. Günter *et al.*, Phys. Rev. B **86**, 235418 (2012).
[11] A. Savoia *et al.*, Phys. Rev. B **80**, 075110 (2009).
[12] B. Kalisky *et al.*, Nat. Mater. **12**, 1091 (2013).
[13] S. A. Pauli *et al.*, Phys. Rev. Lett. **106**, 036101 (2011).
[14] W. Siemons, G. Koster, H. Yamamoto, W. A. Harrison, G. Lucovsky, T. H. Geballe, D. H. A. Blank, and M. R. Beasley, Phys. Rev. Lett. **98**, 196802 (2007).
[15] S. Jyotsna, A. Arora, J. S. Sekhon, and G. Sheet, J. Appl. Phys. **116**, 104903 (2014).
[16] J. Y. Son, J.-H. Lee, and H. M. Jang, Appl. Phys. Lett. **103**, 102901 (2013).
[17] Y. Watanabe, Phys. Rev. B **57**, 789 (1998).
[18] Y. Watanabe, M. Okano, and A. Masuda, Phys. Rev. Lett. **86**, 332 (2001); especially, Fig. 1.
[19] R. A. Cowley, Phys. Rev. **134**, A981 (1964); G. Shirane and Y. Yamada, *ibid.* **177**, 858 (1969); L. Rimai and G. A. deMars, *ibid.* **127**, 702 (1962); K. A. Müller, Phys. Rev. Lett. **2**, 341 (1959).
[20] R. O. Bell and G. Rupprecht, Phys. Rev. **129**, 90 (1963).
[21] H. Unoki and T. Sakudo, J. Phys. Soc. Jpn. **23**, 546(1967).
[22] K. A. Müller and W. Berlinger, Phys. Rev. Lett. **26**, 13 (1971).
[23] A. Okazaki and M. Kawaminami, Mat. Res. Bull. **8**, 545 (1973).
[24] L. Cao, E. Sozontov, and J. Zegenhagen, Phys. Stat. Sol. (a) **181**, 387 (2000).
[25] R. Loetzsch *et al.*, Appl. Phys. Lett. **96**, 071901 (2010).
[26] H. Fujishita, Y. Shiozaki, and E. Sawaguchi, J. Phys. Soc. Jpn. **46**, 581(1979).
[27] P. A. Fleury, J. F. Scott, and J. M. Worlock, Phys. Rev. Lett. **21**, 16 (1968).
[28] H. Uwe and T. Sakudo, Phys. Rev. B **13**, 271 (1976).
[29] Y. Fujii, H. Uwe, and T. Sakudo, J. Phys. Soc. Jpn. **56**, 1940 (1987).
[30] W. J. Burke and R. J. Pressley, Solid State Commun. **9**, 191 (1971).
[31] M. E. Guzhva, V. V. Lemanov, P. A. Markovin and W. Kleemann, Phys. Solid State **39**, 618 (1997).
[32] P. A. Fleury and J. M. Worlock, Phys. Rev. **174**, 613 (1968).
[33] E. Sawaguchi, A. Kikkuchi, and Y. Kodera, J. Phys. Soc. Jpn. **17**, 1666 (1962).
[34] H. Uwe, H. Yamaguchi, and T. Sakudo, Ferroelectrics **96**, 123 (1989).
[35] W. Kleemann, A. Albertini, M. Kuss, and R. Lindner, Ferroelectrics **203**, 57 (1997).
[36] W. Kleemann, U. Bianchi, A. Bürgel, M. Prasse, and J. Dec, Phase Transitions **55**, 57 (1995).
[37] U. Bianchi, W. Kleemann, and J. G. Bednorz, Ferroelectrics **157**, 165 (1994).
[38] H. Uwe, K. B. Lyons, H. L. Carter, and P. A. Fleury, Phys. Rev. B **33**, 6436 (1986).
[39] T. Hashimoto, T. Nishimatsu, H. Izuseki1, Y. Kawazoe, A. Sasaki, and Y. Ikeda, Jpn. J. Appl. Phys. **44**, 7134 (2005).
[40] L. Ni, Y. Liu, C. Song, W. Wang, G. Han, and Y. Ge, Physica B **406**, 4145 (2011).
[41] P. V. Ong and J. Lee, J. Appl. Phys. **112**, 014109 (2012); A. Antons, J. B. Neaton, K. M. Rabe, and D. Vanderbilt, Phys. Rev. B **71**, 024102 (2005).
[42] N. Sai and D. Vanderbilt, Phys. Rev. B **62**, 13942 (2000).
[43] C. LaSota, C.-Z. Wang, R. Yu, and H. Krakauer, Ferroelectrics **194**, 109 (1997).
[44] U. Aschauer and N. A Spaldin, J. Phys.: Condens. Matter **26**, 122203 (2014).
[45] R. Wahl, D. Vogtenhuber, and G. Kresse, Phys. Rev. B **78**, 104116 (2008).
[46] Y. Zhang, J. Sun, J. P. Perdew, and X. Wu, Phys. Rev. B **96**, 035143 (2017).
[47] A. Paul, J. Sun, J. P. Perdew, and U. V. Waghmare, Phys. Rev. B **95**, 054111 (2017).
[48] D. I. Bilc, R. Orlando, R. Shaltaf, G.-M. Rignanese, J. Íñiguez, and Ph. Ghosez, Phys. Rev. B **77**, 165107 (2008).
[49] Y. Watanabe, J. Chem. Phys. **148**, 194702 (2018).
[50] R. Wördenweber, E. Hollmann, R. Kutzner, and J. Schubert, J. Appl. Phys. **102**, 044119 (2007).
[51] J. P. Perdew, A. Ruzsinszky, G. I. Csonka, O. A. Vydrov, G. E. Scuseria, L. A. Constantin, X. Zhou, and K. Burke, Phys. Rev. Lett. **100**, 136406 (2008).
[52] J. Heyd, G. E. Scuseria, and M. Ernzerhof, J. Chem. Phys. **118**, 8207 (2003).
[53] J. Paier *et al.*, J. Chem. Phys. **125**, 249901 (2006).
[54] L. Schimka, J. Harl, and G. Kresse, J. Chem. Phys. **134**, 024116 (2011).
[55] J. Tao, J. P. Perdew, V. N. Staroverov, and G. E. Scuseria, Phys. Rev. Lett. **91**, 146401 (2003); J. Sun, M. Marsman, G. I. Csonka, A. Ruzsinszky, P. Hao, Y.-S. Kim, G. Kresse, and J. P. Perdew, Phys. Rev. B **84**, 035117 (2011).
[56] A. I. Liechtenstein, V. I. Anisimov, and J. Zaanen, Phys. Rev. B **52**, R5467 (1995).
[57] J. P. Perdew, K. Burke, and M. Ernzerhof, Phys. Rev. Lett. **77**, 3865 (1996).
[58] P. E. Blöchl, Phys. Rev. B **50**, 17953 (1994).
[59] G. Kresse and J. Hafner, Phys. Rev. B **47**, 558 (1993); G. Kresse and J. Furthmüller, Comput. Mater. Sci. **6**, 15 (1996); Phys. Rev. B **54**, 11169 (1996); G. Kresse and D. Joubert, *ibid.* **59**, 1758 (1999).
[60] H. J. Monkhorst and J. D. Pack, Phys. Rev. B **13**, 5188 (1976).
[61] E. Poindezter and A. A. Giardini, Phys. Rev. **110**, 1069 (1958).
[62] S. Piskunov, E. Heifets, R. I. Eglitis, and G. Borstel, Comput. Mater. Sci. **29**, 165 (2004).
[63] $s_{11} = (C_{11} + C_{12})/(C_{11} - C_{12})(C_{11} + 2C_{12})$ $s_{12} = -C_{12}/(C_{11} - C_{12})(C_{11} + 2C_{12})$.
[64] P. Erhart, A. Klein, D. Åberg, and B. Sadigh, Phys. Rev. B **90**, 035204 (2014).
[65] A. Bussmann-Holder, K. Roleder, and J.-H. Ko, J. Phys. Chem. Solids **117**, 148 (2018).
[66] S. K. Kurtz, Trans. Am. Crystallogr. Assoc. **11**, 63 (1975).
[67] G. Burns and F. H. Dacol, Phys. Rev. B **28**, 2527 (1983).
[68] M. Takagi and T. Ishidate, Solid State Commun. **113**, 423 (2000).
[69] B. Zalar, V. V. Laguta, and R. Blinc, Phys. Rev. Lett. **90**, 037601 (2003).
[70] K.A. Müller, Ferroelectrics **24**, 185 (1980).

[71] S. M. Shapiro, J. D. Axe, G. Shirane, and T. Riste, Phys. Rev. B **6**, 4332 (1972).
[72] H. Takahasi, J. Phys. Soc. Jpn. **16**, 1685 (1961).
[73] Q. Zhang, T. Cagin, and W. A. Goddard III, Proc. Natl. Acad. Sci. USA **103**, 14695 (2006).
[74] S. M. Sze, *Physics of Semiconductor Devices* (Wiley, New York, 1981).
[75] T. Ando, A. B. Fowler, and F. Stern, Rev. Mod. Phys. **54**, 437 (1982).
[76] M. Krčmar and C. L. Fu, Phys. Rev. B **68**, 115404 (2003).
[77] H. P. R. Frederikse and W. R. Hosler, Phys. Rev. **161**, 822 (1967).
[78] H. P. R. Frederikse, W. R. Thurber, and W. R. Hosler, Phys. Rev. **134**, A442 (1964).
[79] K. Uematsu, O. Sakurai, N. Mizutani, and M. Kato, J. Mater. Sci. **19**, 3671 (1984).
[80] Z. Yu and C. Ang, Appl. Phys. Lett. **80**, 643 (2002).
[81] R. Dingle, H. L. Störmer, A. C. Gossard, and W. Wiegmann, Appl. Phys. Lett. **33**, 665 (1978).
[82] J. Mannhart (private communication).
[83] F. Y. Bruno *et al.*, Phys. Rev. B **83**, 245120 (2011).
[84] L. Miao, R. Du, Y. Yin, and Q. Li, Appl. Phys. Lett. **109**, 261604 (2016).
[85] M. Scigaj, J. Gázquez, M. Varela, J. Fontcuberta, G. Herranz, and F. Sánchez, Solid State Ionics **281**, 68 (2015).
[86] Y. Z. Chen *et al.*, Nat. Commun. **4**, 1371(2013).
[87] M. Li *et al.*, J. Appl. Phys. **124**, 145301 (2018).
[88] A. F. Devonshire, Philos. Mag. **40**, 1040 (1949).
[89] N. Yanase, K. Abe, N. Fukushima, and T. Kawakubo, Jpn. J. Appl. Phys. **38**, 5305 (1999).
[90] Suggested by David Vanderbilt at Fundamental Physics of Ferroelectrics and Related Materials 2018, https://www.materialsbydesign.org/ferro2018.
[91] Y. Watanabe, Comput. Mater. Sci. **158**, 315 (2019).
[92] H. Bilz, G. Benedek, and A. Bussmann-Holder, Phys. Rev. B **35**, 4840 (1987).
[93] For example, S. Kurimura and Y. Uesu, J. Appl. Phys. **81**, 369 (1997), and reference therein.
[94] N. Bickel, G. Schmidt, K. Heinz, and K. Müller, Phys. Rev. Lett. **62**, 2009 (1989).
[95] R. I. Eglitis and D. Vanderbilt, Phys. Rev. B **77**, 195408 (2008).
[96] P. W. Lee *et al.*, Nat. Commun. **7**, 12773 (2016).
[97] For example, Y. Watanabe, Y. Matsumoto, H. Kunitomo, M. Tanamura, and E. Nishimoto, Jpn. J. Appl. Phys. **33**, 5182 (1994).